Structural, magnetic, and electronic properties of a GdAsSe single crystal: Experimental and theoretical studies

R. Kalaivanan,[1,*] Balaji Venkatesan,[1,2,3,*] B. Dundi Sri Chandana,[4] Rajesh Kumar Ulaganathan,[1] G. Senthil Murugan,[1] K. Moovendaran,[1] Joydev Khatua,[5] Li-Hsin Su,[6,7] W. Zhou,[8] Xiaofeng Xu,[9] Chia-Seng Chang,[1,2,3] Tien-Ming Chuang,[1] Yoshiyuki Iizuka,[10] I. Panneer Muthuselvam,[11,†] Horng-Tay Jeng,[1,6,12,‡] Kwang-Yong Choi,[5,§] and Raman Sankar[1,‖]

[1]*Institute of Physics, Academia Sinica, Taipei 10617, Taiwan*
[2]*Department of Physics, National Taiwan University, Taipei 10617, Taiwan*
[3]*Nano Science and Technology Program, Taiwan International Graduate Program, Academia Sinica and National Taiwan University, Taipei 11529, Taiwan*
[4]*Department of Physics, School of Basic and Applied Sciences, Central University of Tamil Nadu, Neelakudi, Thiruvarur, 610005 Tamil Nadu, India*
[5]*Department of Physics, Sungkyunkwan University, Suwon 16419, Republic of Korea*
[6]*Department of Physics, National Tsing Hua University, Hsinchu 30013, Taiwan*
[7]*Department of Electro Physics, National Yang Ming Chiao Tung University, Hsinchu 300093, Taiwan*
[8]*School of Electronic and Information Engineering, Changshu Institute of Technology, Changshu 215500, China*
[9]*Department of Applied Physics, Zhejiang University of Technology, Hangzhou 310023, China*
[10]*Institute of Earth Sciences, Academia Sinica, Taipei 10617, Taiwan*
[11]*Department of Physics (MMV), Banaras Hindu University, Varanasi 221005, Uttar Pradesh, India*
[12]*Physics Division, National Center for Theoretical Sciences, Taipei 10617, Taiwan*

(Received 17 July 2023; revised 14 February 2024; accepted 24 April 2024; published 9 May 2024)

We report high-quality single-crystal growth, x-ray diffraction, magnetic susceptibility [$\chi(T,H)$], magnetization [$M(H)$], heat capacity [$C_P(T,H)$], electrical resistivity [$\rho(T,H)$], and electron spin resonance (ESR) measurements of GdAsSe as functions of temperature and magnetic field. We identify an antiferromagnetic phase transition at $T_N \sim 11.9 \pm 0.2$ K and construct magnetic phase diagrams for $H \parallel ab$ and $H \parallel c$ axes based on the $\chi(T,H)$ and $C_P(T,H)$ data. Isothermal $M(H)$ curves along the $H \parallel ab$ direction at 3 K exhibit a field-induced spin orientation at $H_C \sim 3.78$ T. Both $M(H)$ and $\chi(T,H)$ indicate an easy-plane-type anisotropy. The Curie-Weiss analysis of the high-temperature paramagnetic $\chi(T)$ yields a negative Weiss temperature, suggesting dominant antiferromagnetic interactions between the Gd ions. Magnetic entropy reaches 83% of R ln8 at T_N. The presence of residual entropy above T_N and the persistence of ESR critical broadening up to $\sim 3T_N$ alludes to a degree of magnetic frustration in the studied material. The $\rho(T)$ data above T_N is well fitted to the Bloch-Grüneisen theory for metals. Further, density functional theory calculations reveal an antiferromagnetic ground state where the Gd atoms are coupled ferromagnetically in the *ab* plane and antiferromagnetically along the *c* axis.

DOI: 10.1103/PhysRevB.109.184420

I. INTRODUCTION

In condensed matter physics, rare-earth ($4f$) compounds have garnered considerable interest due to their diverse magnetic and electrical properties, including charge density waves, heavy fermions, and superconductivity [1–6]. The mutual interaction between lattice, spin, and charge plays a crucial role in tuning an electronic band structure in rare-earth-based materials, achieving nontrivial band topology. This intricate interplay of magnetism with or without spin-orbit coupling (SOC) and electron-band topology [7–14] leads to diverse electronic states, ranging from metal and semimetal to insulators and narrow and wide-gap semiconductors [15–20]. In particular, antiferromagnetic $4f$ compounds along with topological semimetals or semiconductors hold immense potential in quantum computing, dissipationless electronic transport, and future spintronic applications due to their inherent stability, reduced energy consumption, and precise control over spin orientations [17,21–26]. Recently, rare-earth-based RB_6X_6 compounds (B = transition elements; X = Si, Ge, Sn) exhibit a myriad of novel quantum states such as large anomalous Hall effects, Chern topological magnetism, and a cycloidal spin structure [27–32].

Despite that the structural and physical properties of ternary rare-earth metal arsenide selenides *MA*Se (M = Pr, Nd, Sm, Gd-Tm, Lu, and A = As, Sb) have been the subject of intense study over the past few decades, a specific subclass of *MA*Se compounds has recently sparked renewed interest due to the discovery of exotic magnetic phases exhibiting topological states, as observed in GdSbTe, CeSbTe, and CeSbSe [33,34]. Most *LnYX* compounds (*Ln* = rare-earth elements,

*These authors contributed equally to this work.
†Corresponding author: ipmphysics@gmail.com
‡Corresponding author: jeng@phys.nthu.edu.tw
§Corresponding author: choisky99@skku.edu
‖Corresponding author: sankarndf@gmail.com

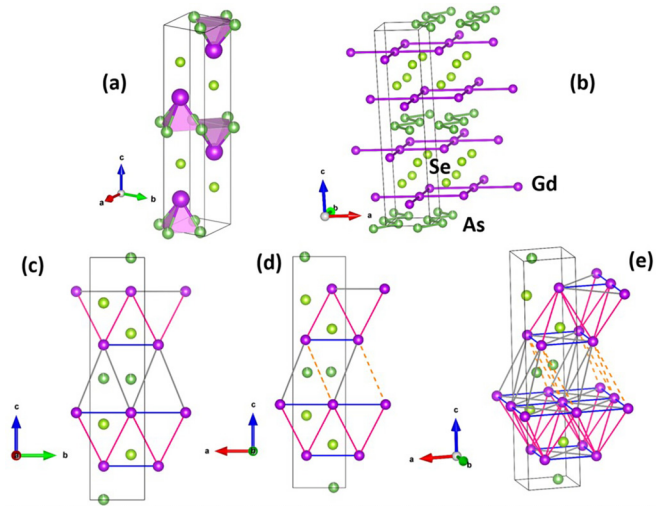

FIG. 1. (a) Crystal structure of GdAsSe. (b) Magnetic Gd atoms form a square-lattice layer in the *ab* plane and As atoms constitute a zigzag chain along the *c* axis. Different view perspectives of unequal triangular lattices (c)–(e) along the *a* axis (c) and the *b* axis (d).

Y = pnictogen, and X = As, Sb) crystallize in a tetragonal PbFCl-type structure [35]. In sharp contrast, Schmelczer *et al.* [36] studied the structural and magnetic properties of GdAsSe, which possesses a monoclinic CeAsS-type structure with the space group $P112_1/n$ and observed antiferromagnetic transitions $T = 10-13$ K in a series of $GdAs_{1-x}Se$ samples. Previous theoretical investigations on related materials have also reported Weyl and Dirac states in CeSbTe [34], an antiferromagnetic semiconductor in *Ln*AsTe [37], magnetic topological semimetal in GdBiTe [38], and gapless nodal-line states in NdSbTe [39].

As shown in Fig. 1, the GdAsSe structure consists of stacked layers of As, Gd, and Se along the *c* axis, arranged in an alternating As-Gd-Se-Se-Gd-As sequence. The distance between the two As layers is approximately 2.7 times larger than that between the Se atom layers (∼3.55 Å). Each Gd atom is surrounded by four As and Se atoms, forming a trigonal prism. The crystal structure comprises a zigzag chain of the As atoms along the *b* axis with a distance of 2.66 Å, and the Gd atoms form a square-lattice arrangement in the *ab* plane. Furthermore, the Gd atoms are sandwiched in two different sequences: Gd-As-Gd and Gd-Se-Se-Gd. The distance between the Gd atoms separated by two nonmagnetic Se layers is shorter than that between a single As layer. The magnetic Gd ion has a magnetic moment of the spin-only value (spin $S = 7/2$ and $L = 0$), resulting in a strong quenching of the crystal field effect due to the absence of SOC. Further, a network of the Gd^{3+} ions is particularly intriguing with respect to the formation of an unequal triangular lattice along both the *c* axis and the *ab* plane. While the basic magnetic properties of GdAsSe have been reported in the literature, detailed magnetic and thermodynamic characterizations on single-crystal or powder samples are currently lacking. Therefore, further investigations are necessary to explore the ramifications of the frustrated connectivity of the Gd ions.

Herein, we comprehensively investigate the structural, magnetic, and thermodynamic properties of a GdAsSe single crystal. We find that GdAsSe undergoes an antiferromagnetic (AFM) phase transition at low temperatures, evident from $\chi(T)$ and $C_P(T)$ measurements as well as supported by density functional theory (DFT) calculations. The A-type antiferromagnetic (A-AFM) magnetic ground state is determined through DFT total energy calculations for various magnetic configurations and the underlying magnetism is further analyzed by calculating exchange parameters based on the Heisenberg model. Our results reveal an easy-plane-type anisotropy through the observation of a field-induced spin-flop transition in the magnetization curve for $H||ab$ at $T = 2$ K. DFT calculations of magnetocrystalline anisotropy energy (MAE) further confirm in-plane magnetization anisotropy consistent with our experimental findings. The critical broadening of the electron spin resonance (ESR) signals, extending beyond several times the Curie-Weiss temperature, showcases the presence of some degree of frustration in GdAsSe, but not of significant magnitude.

II. EXPERIMENTAL DETAILS AND COMPUTATIONAL METHOD

Single crystals of GdAsSe were grown by the chemical vapor transport (CVT) method using I_2 as the vapor transport agent. Initially, the precursor powder materials were mixed with a stoichiometric amount of 5–6 N pure elements in the molar ratio of Gd : As : Se = 1 : 1 : 1. The mixed precursors were placed into a quartz ampoule, which was then evacuated and sealed and gradually heated up to 650 °C, and subsequently maintained at 950 °C for 4 days. Then, the prereacted GdAsSe powder (approximately 10 g) along with the transport solid I_2 agent (purity 4 N) was loaded at one end of the specially designed silica ampoule, which was 43 cm long with an inner diameter of ∼2.0 cm and an outer diameter of 2.2 cm, for the CVT crystal growth. The loaded ampoule was then evacuated and flame-sealed before being placed into a two-zone tube furnace. The prereacted material, in conjunction with I_2, was held at 1050 °C and the growth end was maintained at 950 °C for 10 days. Finally, a thin plate of GdAsSe single crystals with approximate dimensions of $1.5 \times 1.5 \times 1\text{mm}^3$ was obtained.

Room-temperature x-ray diffraction (XRD) measurements were performed using a D8 diffractometer with Cu $K\alpha$ radiation. The structural analysis was carried out by Rietveld refinement using the FULLPROF software. The composition of the single crystal was analyzed by the electron probe microanalyzer (EPMA) technique. Magnetic measurements were conducted using a vibrating sample magnetometer (Quantum Design). A physical property measurement system was employed to measure heat capacity, $C_P(T, H)$, as a function of temperature by the relaxation method. ESR spectra were recorded on an *X*-band electron paramagnetic resonance spectrometer (EMXplus-9.5/12/P/L system) in the temperature range of $T = 17-293$ K.

First-principles electronic structure calculations were performed using the Vienna *ab initio* simulation package (VASP) [40,41] based on DFT. The exchange-correlation functional in the generalized gradient approximation [42] as described by the Perdew-Burke-Ernzerhof (PBE) [43] form was adopted in our calculations. Rotationally invariant PBE plus Hubbard *U*

TABLE I. PBE + U + SOC optimized Wyckoff positions of GdAsSe using experimental lattice constants $a = 4.0154$ Å, $b = 3.9689$ Å, and $c = 17.3719$ Å obtained in this work.

Atom	Multiplicity	Wyckoff letter	Site symmetry	Coordinates		
				x	y	z
Gd	2	A	$mm2$	0.25	0.25	0.28033
As	2	B	$mm2$	0.25	0.75	0.99989
Se	2	A	$mm2$	0.25	0.25	0.62802

[44] (PBE+U) with the effective on-site Coulomb repulsion $U = 6.7$ eV and exchange interaction $J = 0.7$ eV [45] was taken into account for addressing strong correlation in the localized Gd f orbital. The $U = 6.7$ eV is given by fitting the L(S)DA+U results with experimental spectra [45]. In this work, we have fitted the PBE+U results with experimental spectra [45] and confirm that $U = 6.7$ eV gives best-fit results similar to previous L(S)DA calculations [45]. Furthermore, the SOC effect was self-consistently included in the PBE calculations (PBE + SOC, PBE + U + SOC). The experimental lattice constants $a = 4.0154$ Å, $b = 3.9689$ Å, and $c = 17.3719$ Å obtained in this work were used for DFT atomic position relaxation until the residual force is less than 0.01 eV/Å. The optimized Wyckoff positions are given in Table I.

For MAE total energy calculations, we utilized PBE + U + SOC calculations to determine the magnetic ground state A-AFM using the $18 \times 18 \times 3k$ mesh over the Brillouin zone with an energy cutoff of 600 eV under the energy convergence criterion of 10^{-6} eV. The MAE is the total energy difference between in-plane and out-of-plane magnetizations $E[100]-E[001]$. To resolve the magnetic ground state, a higher $22 \times 22 \times 6k$ mesh with an energy cutoff of 700 eV and an energy convergence criterion of 10^{-6} eV were employed in total energy calculations for four possible magnetic configurations: A-AFM, AFM 1, AFM 2, and FM. Exchange interactions were further deduced through exchange parameter calculations using the Heisenberg model [46], based on DFT total energies.

III. RESULTS AND DISCUSSION

A. Crystallography

The x-ray powder diffraction was recorded on both a single crystal [Fig. 2(a)] and crushed single-crystal powder of GdAsSe at room temperature. The Rietveld refinement fitting of the powder is shown in Fig. 2(b). The XRD analysis of a GdAsSe single crystal shows reflections of the (00l) plane. The strong and sharp reflections indicate the high quality of grown crystals. The Rietveld refinement results confirm that GdAsSe crystallizes in the monoclinic crystal structure with space group $P112_1/n$. The absence of impurity traces demonstrates the high-purity nature of the grown GdAsSe crystals. The results of the refined fit parameters yield a goodness of fit $\chi^2 = 2.79$, $R_p = 5.84\%$, and $R_{wp} = 8.03\%$. Moreover, the obtained lattice parameters are $a = 4.0154(3)$ Å, $b = 3.9689(2)$ Å, and $c = 17.3719(6)$ Å, in agreement with the previously reported values [36]. The EPMA measurements

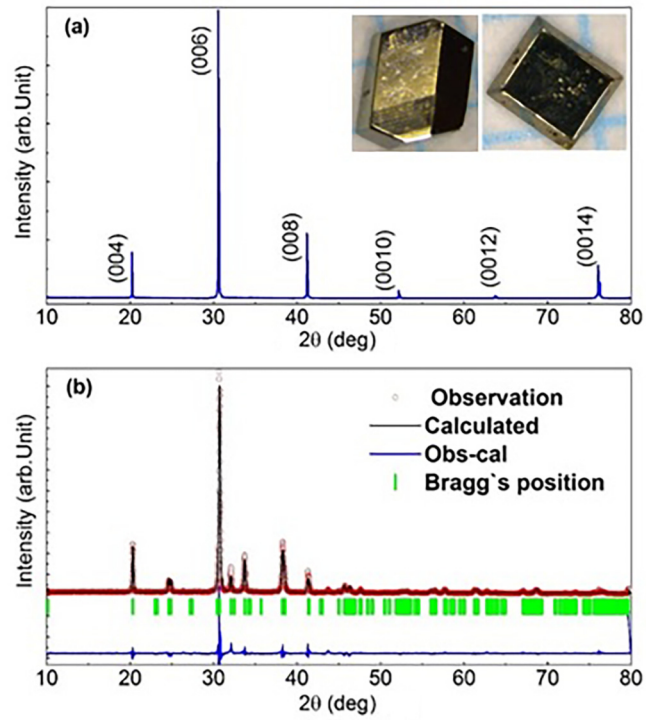

FIG. 2. (a) X-ray diffraction pattern of a single crystal of GdAsSe. (b) Rietveld refinement of x-ray diffraction data on a crushed single-crystals powder of GdAsSe.

were performed on several spots on a single crystal and different batches of the grown GdAsSe crystals. The results confirm the homogeneity of the grown crystals with an average expected composition of Gd : As : Se = 1 : 1 : 1 (1:0.89:1) within the errors. No other metal elements were detected in these crystals, except for the presence of Gd, As, and Se elements.

B. Atomic resolution surface topography

To further assess the quality of our samples, scanning tunneling microscopy (STM) measurements were performed on a GdAsSe single crystal by using a homemade low-temperature STM system [47] with an electrochemically etched tungsten tip. The sample was first cooled down below $T \sim 30$ K and then cleaved *in situ* under cryogenic ultrahigh-vacuum conditions. Subsequently, it was immediately transferred to the STM head for measurements at $T = 4.5$ K. Because of its layered structure and crystalline symmetry, cleavage is expected to occur between Se planes, yielding a charge-natural surface.

Figures 3(a) and 3(b) show STM topography of the Se-terminated surface taken with a sample bias voltage of -2 V and the corresponding Fourier-transformed image, respectively. Several clusters with sizes of several nanometers (indicated by yellow circles) can be observed on the surface, which are likely adatoms resulting from the violent cleavage process. Single-atom vacancies at the Se sites (indicated by yellow arrows) are visible in the STM image, which corresponds to less than 1% of Se vacancies on the surface. A few impurities, which appear as bright spots (indicated by the red arrow) in Fig. 3(a), also exist at the Gd sites. Interestingly,

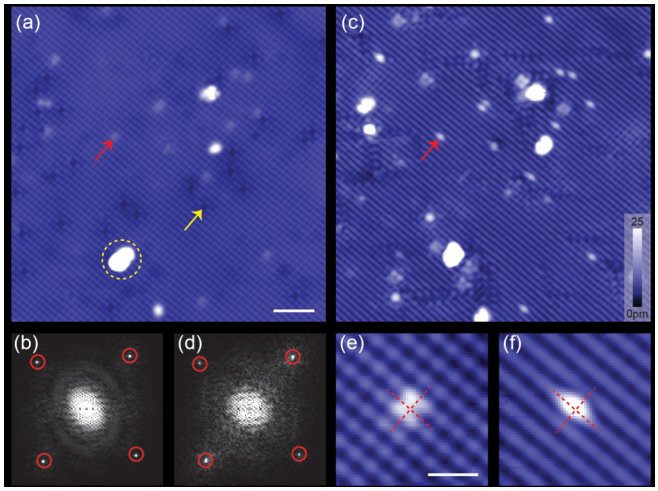

FIG. 3. STM images of GdAsSe. (a) Topographic image taken on the cleaved GdAsSe surface revealing the Se lattice (bias voltage, $V = -2$ V; current set point, $I = 20$ pA and $T = 4.5$ K). The scale bar represents 3 nm. The dotted yellow circle, the yellow arrow, and the red arrow denote adatoms arising from the cleavage process, a Se vacancy, and a Gd impurity, respectively. (b) Corresponding Fourier-transformed image of (a). (c) Topographic image taken in the same field of view as in (a) with bias voltage, $V = 1$ V. The red arrow denotes the same impurity in (a). (d) Corresponding Fourier-transformed image of (c). The red circles mark the Bragg peaks in (b) and (d). (e) and (f) Enlarged image centered at the Gd impurity marked by a red arrow in (a) and (b), respectively. The red crosses indicate the impurities location as a reference. The scale bar is 1 nm.

when applying a bias voltage of 1 V, the STM image taken in the same field of view reveals the Gd lattice underneath the Se-terminated surface, as shown in Fig. 3(c). The contrast shift along the *a* and *b* axes in STM images is more evident from the enlarged images centered at a Gd impurity. The impurity site denoted by a red cross is located at the center of four Se atoms on the Se surface in Fig. 3(e) and appears on the Gd site in Fig. 3(f). The As layer, which is oriented ∼45 ° with respect to the Gd and Se layers, is not observed in our images, different from a previous STM study on ZrSiS [48]. The observation of both Se and Gd layers at two different bias voltages indicates a change in the density of states contribution to the charge density from Se and Gd atoms within the energy range of our STM measurements. Our STM images along with XRD and EPMA measurements confirm the high quality of our GdAsSe single crystals, enabling further characterizations.

C. Magnetic susceptibility and magnetization

Figure 4(a) presents the zero-field-cooled (ZFC) and field-cooled (FC) magnetic susceptibility $\chi(T) = M/H$ data of GdAsSe single crystal measured at $\mu_0 H = 0.01$ T applied along the *c* axis and the *ab* plane. No hysteresis and bifurcation are observed between the ZFC and FC curves of $\chi(T)$. With decreasing temperature, $\chi(T)$ steeply increases and shows a distinct peak feature at $T_N \sim 11.9$ K. As evident from the plot of $d\chi(T)/dT$ versus temperature in Fig. 4(b), the anomaly signifies the occurrence of an antiferromagnetic phase transition. Below T_N, $\chi(T)$ exhibits a strong directional dependence. Specifically, for $H||ab$, $\chi(T)$ shows a rapid drop, while $\chi(T)$ remains largely temperature independent for $H||c$. This disparate behavior of $\chi(T < T_N)$ data between $H||c$ and $H||ab$ points to the easy-plane-type anisotropy, with the magnetic moment predominantly aligned within the *ab* plane. We note that MAE calculations were conducted for the A-AFM magnetic ground state using PBE + U + SOC total energy calculations with SOC included self-consistently for out-of-plane (E[001]) and in-plane (E[100]) magnetizations. The convergent MAE (E[100]− E[001]) of −0.02 meV/cell indicates the easy-plane-type anisotropy, in line with our experimental results, as illustrated in Fig. 4.

Above $T \geqslant 20$ K, the observed $\chi(T)$ follows the Curie-Weiss law, $\chi(T) = C/(T - \theta)$, where C and θ are the Curie constant and the Curie-Weiss temperature, respectively. Fitting the data between 20 and 300 K gives $C = 7.86$ cm^3 K/mol and $\theta = -17.8$ K for $H||c$ and $C = 7.82$ cm^3 K/mol and $\theta = -18.4$ K for $H||ab$. The effective magnetic moments deduced from the Curie constant are 7.93 μ_B for $H||c$ and 7.91 μ_B for $H||ab$, which are close to the expected spin-only value of ∼7.94 μ_B (Gd^{3+}:$S = 7/2$, $L = 0$) [4]. The negative sign of θ indicates the dominance of antiferromagnetic interactions between the Gd^{3+} moments. The similar magnitude between T_N and θ suggests that GdAsSe is not subject to frustration and behaves like a classical magnet due to its large spin number.

To further explore the magnetic phase transitions of the GdAsSe single crystal, $\chi(T)$ was measured under different applied magnetic fields. The field and temperature evolution of $\chi(T)$ for $H||ab$ and $H||c$ is shown in Figs. 4(c) and 4(d), respectively. As the applied magnetic field increases, the magnetic phase transition T_N shifts to lower temperatures for both orientations, consistent with observations reported in many conventional AFM systems [4,49,50]. More specifically, when an external magnetic field is applied, the Zeeman energy acting on the magnetic moments forces their alignment with the field. As the field strength increases, a greater number of magnetic moments align with the field direction, resulting in a weakening of the antiferromagnetic order and, consequently, a reduction in the Néel temperature.

The isotherm magnetization $M(H)$ versus applied magnetic field measured at different selected temperatures is shown in Fig. 5 for the $H||ab$ plane and in the inset of Fig. 5 for $H||c$. The $M(H)$ curve shows a linear increase with applied magnetic field for $H||c$, as expected for AFM systems (shown in the inset of Fig. 5). In contrast, the $M(H)$ curve for $H||ab$ features a distinct jump at 3.8 T, which is assigned to a spin-flop (SF) transition. Noteworthy is that neither of the $M(H)$ curves saturates in either direction. The magnetization value of ∼(2.78–3.2)μ_B at $\mu_0 H = 7$ T is smaller than the saturation magnetic moment $\mu_{sat} = gS\mu_B/\text{Gd} = 7\,\mu_B/\text{Gd}$, where $S = 7/2$, $L = 0$, and $g = 2$. From a simple extrapolation, we expect that the saturation field will be in the range of ∼(15–17) T, which is comparable to the Curie-Weiss temperature θ.

To trace the thermal evolution of the SF transition, we plot the dM/dH versus $H||ab$ in Fig. 5 (right axis). The sharp peak in dM/dH alludes to a first-order phase transition and confirms that GdAsSe has an easy-plane anisotropy along the *ab* plane. Further, it is observed that the SF transition slightly shifts towards higher magnetic fields with increasing temperature.

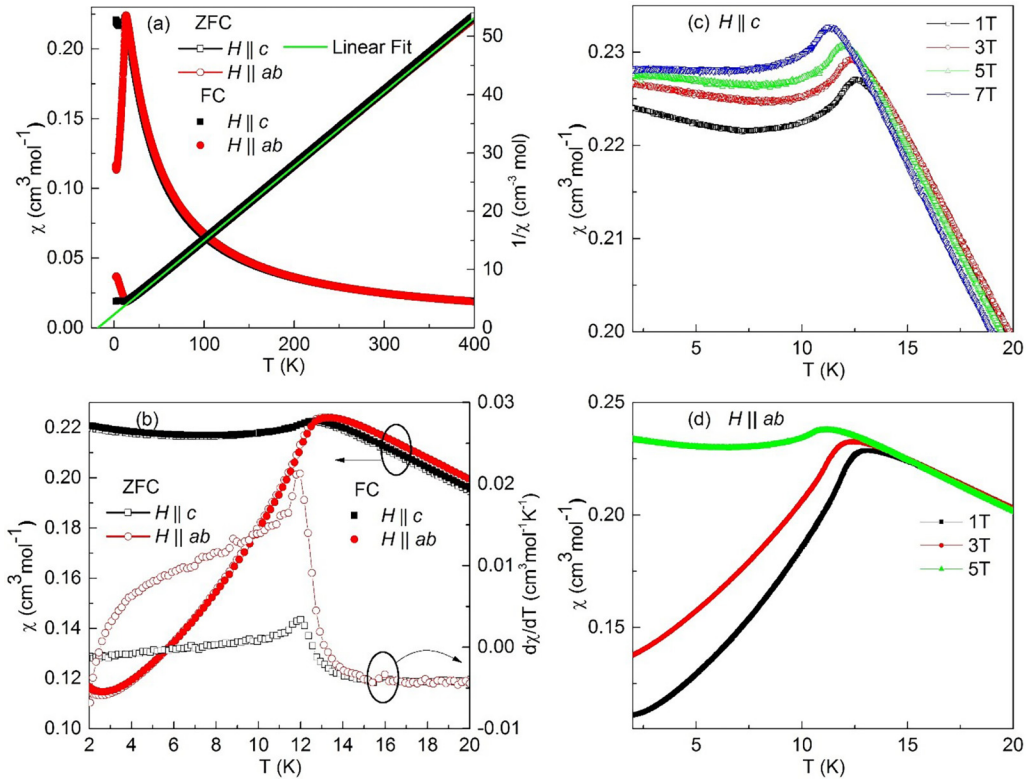

FIG. 4. (a) Zero-field-cooled (ZFC) and field-cooled (FC) magnetic susceptibility of GdAsSe single crystal (left axis) and its reciprocal magnetic susceptibility for ZFC data (right axis) as a function of temperature at an applied magnetic field of 0.01 T for $H||ab$ and $H||c$. The green solid line is the Curie-Weiss law fit of the $T = 20-300$ K data to $\chi(T) \sim C/(T-\theta)$. (b) An enlarged view of the magnetic susceptibilities at the vicinity of T_N (left axis) and its derivatives for the ZFC data (right axis). The magnetic susceptibility versus temperature under various applied magnetic fields (c) for $H||c$ and (d) $H||ab$.

D. Heat capacity

Figure 6 shows the temperature dependence of the heat capacity $C_P(T,H)$ for a single crystal of GdAsSe measured for $H||c$ in zero magnetic field and at various applied magnetic fields (inset of Fig. 6). A distinct λ-like anomaly is seen in C_P at 11.9 K, in excellent agreement with the $\chi(T)$ data. With increasing magnetic fields along the c axis, the phase transition temperature T_N shifts to lower temperatures. Additionally, the magnitude of $C_p(T)$ decreases with increasing magnetic fields. In the temperature range of $T = 22-37$ K, lying above T_N, we attempted to analyze C_P in terms of the conventional expression $C_p(T) = \gamma T + \beta T^3$, where γ is the Sommerfeld coefficient associated with the conduction electrons and β is the lattice coefficient. A linear fit yields the value of $\gamma \sim 324$ mJ mol^{-1} K^{-2} and $\beta \sim 0.3$ mJ mol^{-1} K^{-4}. The Debye temperature, $\theta_D = (12\pi^4 nR/5\beta)^{1/3} \sim 269$ K is extracted from the β value.

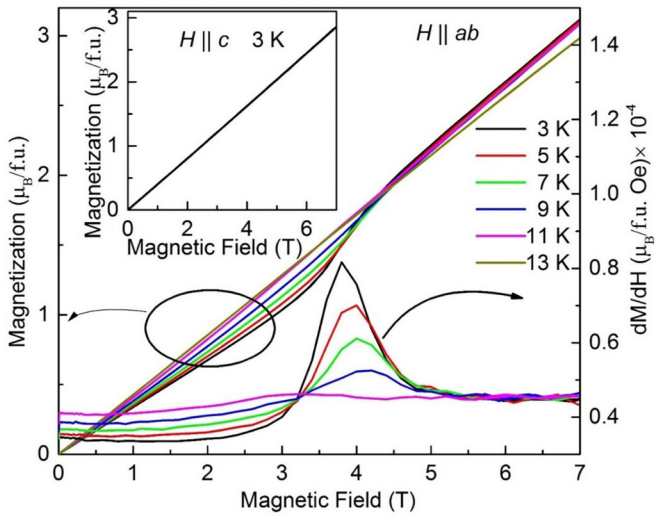

FIG. 5. Field dependence of the magnetizations measured at different selected temperatures along the $H||ab$ plane and their derivatives (right axis). The inset shows the magnetization curve for $H||c$ measured at $T = 3$ K.

In order to isolate the lattice phonon contribution from the C_P data, the Debye model for the lattice heat capacity plus γT is used to fit in the temperature range between 19 and 215 K [4]:

$$C_{ph} = 9nR\left(\frac{T}{\theta_D}\right)^3 \int_0^{\theta_D/T} \frac{x^4 e^x}{(e^x-1)^2} dx + \gamma T,$$

where n is the number of atoms per formula unit, R is the molar gas constant, and θ_D is the Debye temperature. The best fitting yields $\theta_D \sim 250(3)$ K and $\gamma \sim 316$ mJ mol^{-1} K^{-2}.

The magnetic contribution to $C_P(T,H)$ is deduced from the expression $C_{mag} = C_p - C_{ph}$. The resulting C_{mag} is shown in Fig. 6(b). Furthermore, the magnetic entropy (S_m) is estimated by integrating C_{mag}/T and is shown on the right axis of

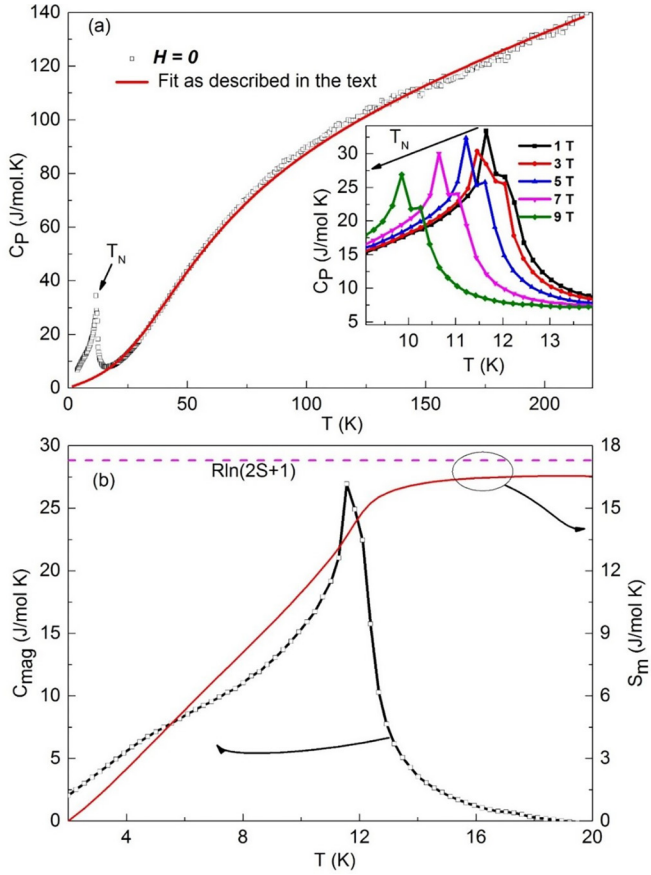

FIG. 6. (a) Temperature dependence of $C_P(T,H)$ along the c axis for GdAsSe at $\mu_0 H = 0$ T. The inset depicts $C_P(T,H)$ at various selected applied magnetic fields. The solid red line corresponds to the fitting as described in the text. (b) Magnetic specific heat $C_{mag}(T,H)$ versus temperature in the left axis and the magnetic entropy S_m versus temperature in the right axis.

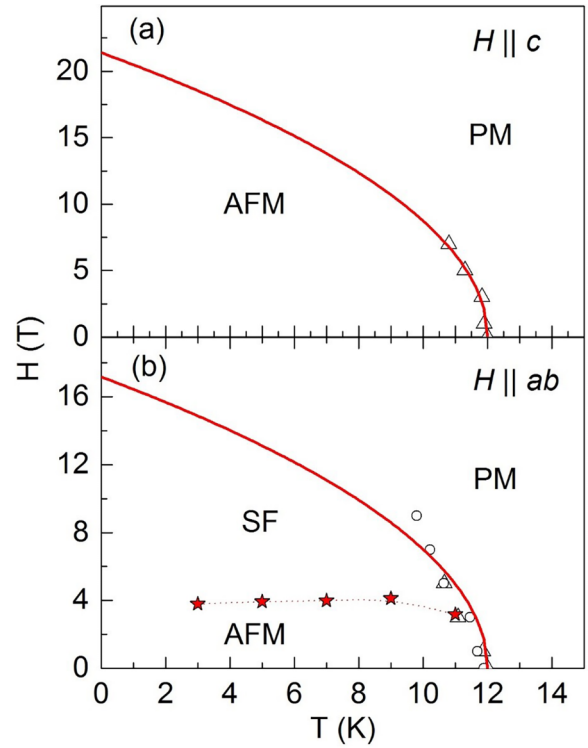

FIG. 7. The T-H magnetic phase diagrams drawn from the $\chi(T,H)$ (open triangular symbols) and $C_P(T,H)$ data (open circular symbols). The red solid curve is a fitting curve to the equation $H = H_0[1 - T_N(H)/T_N(H = 0)]^{0.5}$.

Fig. 6(b). As the temperature increases, S_m reaches a saturated value of ∼16.56 J/mol K, just above T_N. The saturated value is in fairly good agreement with the theoretically expected total magnetic entropy $S_m = R\ln(2S + 1) = 17.285$ J/molK for Gd^{3+} ($S = 7/2$). At T_N, the S_m reaches 83% of R ln8 and the remaining entropy is accounted for at temperatures below 2 K.

Both $M(H)$ and $\chi(T)$ give evidence that the magnetic moments in GdAsSe are aligned antiferromagnetically in the ab plane, suggesting collinear AFM or coplanar noncollinear AFM along the ab plane [51,52]. Despite the presence of unequal triangular lattices in the ab plane and along the c axis, we find no signature of magnetic frustration. This lack of frustration is primarily attributed to the large difference of exchange interactions even with different sign as well as a large spin number (see Table II). Moreover, the obtained negative, small Curie-Weiss constant indicates the presence of moderate AFM interactions. Further, we stress that the orbital moment in this compound is quenched ($L = 0$).

E. Magnetic phase diagrams

Figure 7 presents the T-H phase diagrams, which are constructed based on the $\chi(T,H)$ and $C_P(T,H)$ data for both the $H||c$ and the $H||ab$ directions. As evident from both $\chi(T,H)$ and $C_P(T,H)$ data, T_N shifts to lower temperatures with increasing magnetic field. For $H||c$, the applied field induces a simple transition from an AFM to a paramagnetic (PM) phase. However, for $H||ab$, the phase transition involves three distinct phases: AFM phase, SF phase, and PM phase.

The shift of T_N in both cases can be fitted to the equation $H = H_0[1 - T_N(H)/T_N(H = 0)]^{0.5}$ [4], where H_0 is the

TABLE II. Total energies of the four magnetic arrangements in Fig. 10 obtained from PBE, PBE+U, PBE+SOC, and PBE + U + SOC calculations. The total energy of the nonmagnetic state is much higher and hence is not listed here.

$U = 6.7$ (eV), $J = 0.7$ (eV)	A-AFM	AFM 1	AFM 2	FM
PBE (eV/cell)	−106.40326	−106.40318	−106.39595	−106.39935
PBE+U (eV/cell)	−105.47674	−105.47602	−105.43917	−105.43471
PBE+SOC (eV/cell)	−108.89046	−108.89022	−108.88339	−108.88757
PBE + U + SOC (eV/cell)	−108.19288	−108.19237	−108.17179	−108.16737

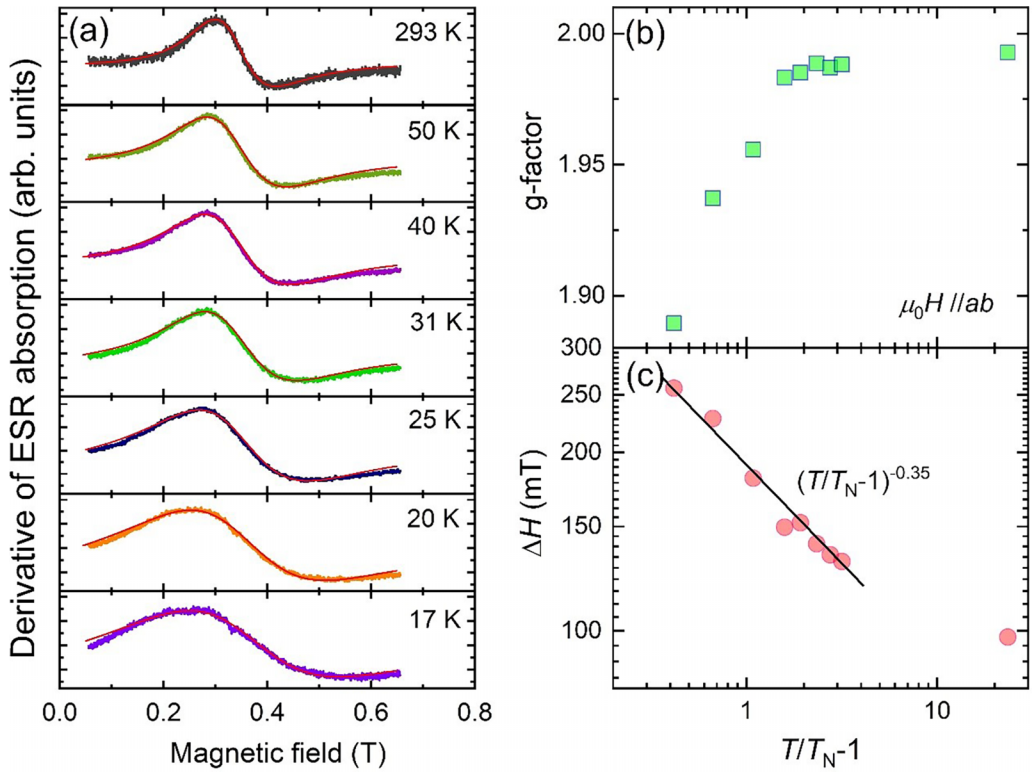

FIG. 8. (a) Derivative of the ESR absorption spectra at selected temperatures for $H||ab$. The ESR spectra are fitted to a Dysonian profile (solid lines). (c) Semilogarithmic plot of the g factor as a function of reduced temperature. (c) Log-log plot of the ESR linewidth ΔH vs reduced temperature. The solid line represents a power-law fit.

critical magnetic field. The fitting yields $\mu_0 H_0 \sim 17.2$ T and $\sim$21.4 T for $H||ab$ and $H||c$, respectively. The lower value of H_0 along the ab plane supports the notion of an easy-plane anisotropy along the $H||ab$ direction. Further, we note that the estimated critical fields are comparable to the anticipated saturation fields extrapolated from the magnetization curves shown in Fig. 5.

F. Electron spin resonance

To gain insights into the thermal evolution of spin correlations, we employed an ESR technique. Figure 8(a) exhibits the X-band ESR spectra measured over a temperature range of $T = 17-293$ K. With decreasing temperature, the ESR signal progressively broadens and shifts to lower fields. Below T_N, no ESR signal is detectable, indicating that a magnon gap exceeds the X-band frequency. In the high-temperature paramagnetic state, the ESR spectrum exhibits an asymmetrical and broad profile that can be described by a Dyson function. This Dysonian line profile comprises a Lorentzian component broadened by a Gaussian distribution. The Lorentzian contribution arises from intrinsic line broadening caused by spin-spin interactions and relaxation processes. Conversely, the Gaussian component originates from inhomogeneous broadening due to spatial variations in the local environment or magnetic field experienced by the paramagnetic ions. In the case of low-resistivity semiconductors, such as the compound under investigation, samples with dimensions larger than the skin depth bring about a nonuniform distribution of the microwave field within the sample. For GdAsSe, we determined the asymmetry parameter, which quantifies the ratio of dispersion to absorption, to be $\alpha = 0.4-0.6$.

Shown in Figs. 8(b) and 8(c) are the temperature dependencies of the g factor and the linewidth, ΔH, respectively. At room temperature, the in-plane effective g factor is determined to be $g_{ab} = 1.99(2)$. With decreasing temperature from $1.6T_N$, g_{ab} decreases to a value of 1.88(9). The decrease in the in-plane g factor is associated with the increase of a local staggered internal field. For temperatures below $\sim 3T_N$, we observe that $\Delta H(T)$ follows a critical power law $(T/T_N - 1)^{-0.35\pm0.02}$ for $H||ab$. This critical-like line broadening arises from the development of in-plane short-range spin correlations. We note that the onset temperature of the short-range correlations corresponds to $\sim(2–3)\theta$, as deduced from the Curie-Weiss fits, suggesting the presence of some degree of magnetic frustration, although it is not significantly pronounced.

G. Electrical resistivity

Figures 9(a) and 9(b) show the electrical resistivity as a function of temperature from $T = 2$ to 300 K at $\mu_0 H = 0$ T and selected magnetic fields, respectively. At $\mu_0 H = 0$ T, the residual resistivity ρ_0 at 2 K is 1.08 mΩ cm, and the residual resistivity ratio is $\rho(300\ \text{K})/\rho_0 \sim 1.52$. The $\rho(T)$ reveals metallic behavior in the measured temperature range, decreasing linearly with decreasing temperature up to 75 K. Below $T = 75$ K, the decreasing rate is slowly reduced and nearly saturates around 13 K. A sharp drop in $\rho(T)$ occurs at the antiferromagnetic transition $T_N \sim 12$ K on further cooling.

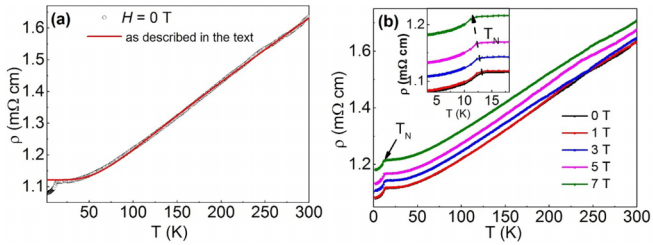

FIG. 9. Electrical resistivity ρ of GdAsSe as a function of temperature without an external magnetic field (a) and measured in selected magnetic fields (b). The inset of shows the field dependence of T_N.

This behavior is observed in both heating and cooling modes of measurements with no discernible hysteresis, indicative of a second-order transition. The obtained resistivity values of $\rho \sim 1.08$–1.64 mΩ cm suggest a semimetallic nature, compared to the order of $\mu\Omega$ cm in normal metals. The abrupt drop in $\rho(T)$ is attributed to the magnetic origin, signifying a reduction in spin-disorder scattering below T_N.

Above T_N, the $\rho(T)$ data are fitted by the Bloch-Grüneisen (BG) model where the resistivity arises from electron-phonon scattering, as given by [4]

$$\rho_{BG} = \rho_0 + F\left(\frac{T}{\theta_R}\right)^5 \int_0^{\theta_R/T} \frac{x^5 dx}{(1-e^{-x})(e^x-1)},$$

where F is a numerical constant and θ_R is the resistively determined Debye temperature. The red solid line in Fig. 9(a) illustrates the best fit to the data, with the fit yielding $\theta_R \sim 365$ K. We also measured the $\rho(T)$ under various applied magnetic fields. As observed in $\chi(T)$ and $C_P(T)$ measurements, the T_N in $\rho(T)$ shifts to lower temperatures with increasing magnetic fields. The magnitude of resistivity experiences an increase proportional to the applied magnetic field.

H. Computational results

In this work, we examined four magnetic structures of GdAsSe, including A-AFM, AFM 1, AFM 2, and ferromagnetic (FM) states, as shown in Fig. 10. The A-AFM state is characterized by antiparallel spins in alternate Gd layers. In the AFM 1 state, the Gd bilayer exhibits FM spin alignment, while the Gd bilayers on the opposite side of the As layer are coupled antiferromagnetically. Similarly, in the AFM 2 state, spins are arranged ferromagnetically within the Gd-As-Gd trilayer and antiferromagnetically to the next Gd-As-Gd trilayer.

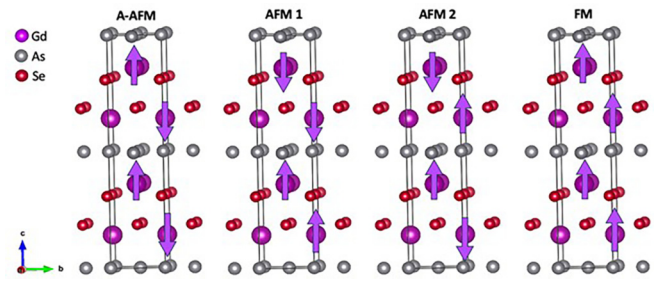

FIG. 10. (a) Illustration of four possible magnetic states: A-AFM, AFM 1, AFM 2, and FM studied in this work. The purple arrows indicate the spin direction of Gd ions.

For the four magnetic configurations, we performed PBE, PBE+U, PBE+SOC, and PBE + U + SOC self-consistent total energy calculations, as listed in Table II for comparison. The nonmagnetic state consistently shows significantly higher total energy, which can be understood by considering the presence of a Gd f orbital in GdAsSe and thus is not listed here. The obtained magnetic moments of Gd ions in all magnetic calculations are close to 7 μ_B as expected for the approximately half-filled Gd f orbital. As evident from the Table II, A-AFM and AFM 1 belong to the lower-energy group with nearly degenerate total energies. Without the inclusion of the on-site U, PBE, and PBE+SOC give nearly degenerate total energies for A-AFM and AFM 1. With U included in PBE+U and PBE + U + SOC calculations, A-AFM shows slightly lower total energy, leading to the magnetic ground state of GdAsSe. On the other hand, for AFM 2 and FM with higher total energy, PBE and PBE+SOC favor the FM state, while calculations with on-site U prefer the AFM 2 state. The relatively higher total energy group, AFM 2 and FM configurations, implies strong superexchange antiferromagnetic coupling within the Gd-As-Gd trilayer. For the lower-energy group, A-AFM and AFM 1, the total energy difference is in sub-meV order. The most accurate PBE + U + SOC calculations reveal that A-AFM constitutes the magnetic ground state with its total energy 0.5 meV lower than that of the AFM 1 state, indicating a very weak antiferromagnetic preference in the Gd-Se-Se-Gd quadlayer. Overall, we conclude that the magnetic ground state of GdAsSe is the A-AFM state with the nearly degenerate AFM 1 state. This tendency toward AFM coupling in the c axis and FM coupling in the ab plane is consistent with the easy-plane-type magnetic anisotropy.

To gain a deeper insight into the magnetism in GdAsSe, we further employed PBE + U + SOC to investigate the exchange parameters between Gd ions: J_1 for the nearest neighbor, J_2 for the next-nearest neighbor, J_3 for the next-next-nearest neighbor, J_4 for the next-next-next-nearest neighbor, and J_5 for the next-next-next-next-nearest neighbor interaction, as illustrated in Fig. 11. J_1 and J_2 are lateral nearest Gd-Gd exchange interactions along the lattice $\boldsymbol{b}$ and $\boldsymbol{a}$ directions, respectively. J_3 represents the interlayer exchange interaction within the Gd-Se-Se-Gd quadlayer sandwiched by As layers. J_4 is the interlayer exchange interaction between Gd-Gd layers spanning across As layers. J_5 denotes the exchange parameter between the lateral next-nearest Gd-Gd. The resultant crucial exchange parameters are $J_3 = -0.032$ (meV/cell) and $J_4 = -1.318$ (meV/cell). The tiny negative J_3 indicates a very weak antiferromagnetic tendency within the Gd-Se-Se-Gd quadlayer, while the significantly larger negative J_4 shows a strong antiferromagnetic coupling in the Gd-As-Gd trilayer. These quantitative results are consistent with the qualitative discussion in the previous paragraph and further provide a solid basis for understanding the magnetism in GdAsSe, thereby supporting our experimental results.

To demonstrate the s, p, d, and f contributions to the electronic structures, we also calculated the atom-decomposed density of state (DOS) of GdAsSe and the orbital-decomposed DOS of the Gd ion from PBE + U + SOC. As shown in

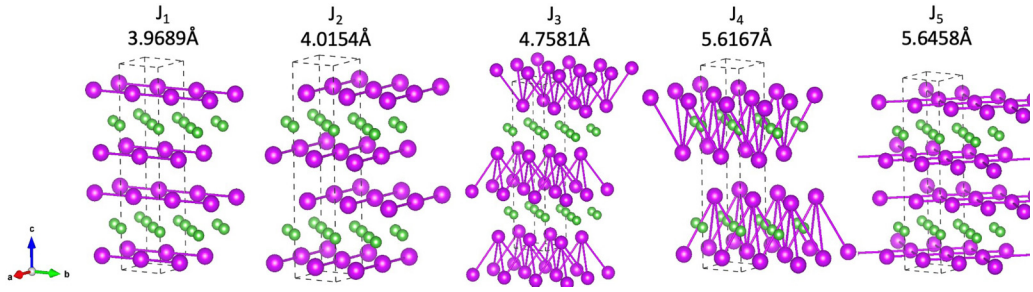

FIG. 11. The exchange parameters J_1, J_2, J_3, J_4, and J_5 are the nearest neighbor, next-nearest neighbor, next-next-nearest neighbor, next-next-next-nearest neighbor, and next-next-next-next-nearest neighbor for Gd-Gd atoms, respectively. Magenta and green spheres indicate Gd and As ions, respectively. The Se ions between Gd layers are neglected for a clear view to J_3.

Fig. 12(a), the spin-up f band of Gd spans from -7 to -8 eV with a high intensity and a narrow bandwidth of about 1 eV, while the spin-down counterpart ranges from 2.5 to 4 eV, indicating the high-spin state of the Gd ion ($\sim$6.9 μ_B) induced by the half-filling f band. Gd also exhibits a spin-up narrow d band from 2.5 to 3.5 eV. All the Gd, As, and Se ions develop a strongly hybridized band from -5 up to 2 eV with approximately the same shape and intensity in both the spin-up and the spin-down channels, demonstrating nonmagnetic behavior in this energy interval. The orbital-decomposed DOS of Gd in Fig. 12(b) illustrates that the aforementioned two sharp narrow bands of Gd are the occupied spin-up and empty spin-down f bands with an exchange splitting of about 12 eV, as can be expected for the f bands with strong magnetism. This Mott gap between the spin-up and spin-down f bands increases to $\sim$12.5 eV with a slightly larger U value of 8.0 eV,

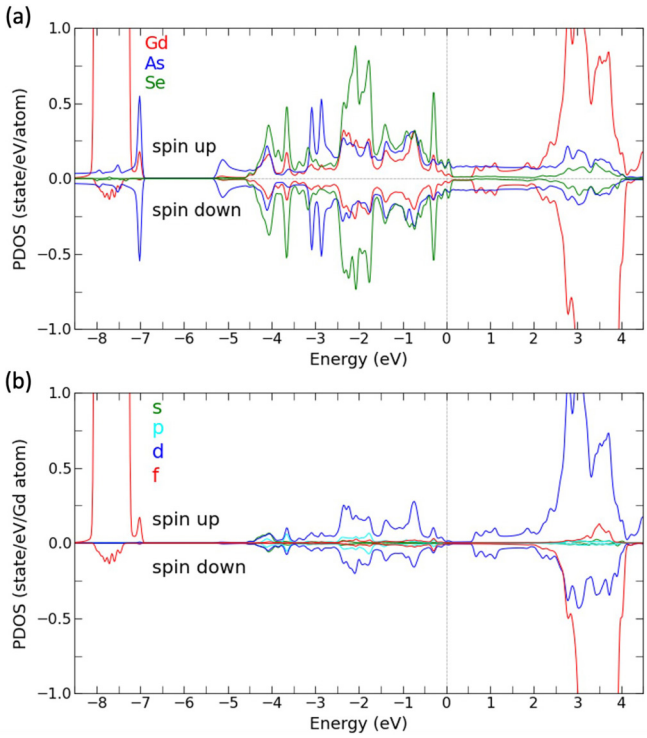

FIG. 12. Atom-decomposed density of state (a) and orbital-decomposed Gd density of state of GdAsSe in the magnetic ground state A-AFM from PBE + U + SOC (b).

and decreases to $\sim$10.5 eV with a slightly smaller U of 6.0 eV. In comparison with the experimental Mott gap of $\sim$12.5 eV [45], the U value of 6.7 eV [45] might be slightly underestimated. The Gd d bands also exhibit spin splitting, with the spin-up d band around 3 eV above the Fermi level and the spin-down d band beyond 4 eV. Since both the spin-up and the spin-down Gd d bands are empty, we thus will not discuss further details here.

IV. CONCLUSION

We have grown successfully high-quality single crystals of GdAsSe and characterized their structural, magnetic, and thermodynamic properties. The magnetic susceptibility and specific heat measurements exhibit an antiferromagnetic phase transition at $T_N = 11.9$ K. The $\chi(T,H)$ and $C_P(T,H)$ measurements reveal that the T_N shifts to lower temperatures with increasing magnetic fields. Moreover, the single-crystal magnetization curve shows a field-induced spin-flop magnetic phase in the ab plane, demonstrating easy-plane-type anisotropy. The entropy reaches 83% of R ln8 at T_N and the in-plane ESR linewidth shows the development of spin-range magnetic correlations, suggesting some degree of magnetic frustration or low-dimensional behavior in the system. The electrical resistivity data reveal metallic behavior and is fitted above T_N using the Bloch-Grüneisen model, which accounts for electron-phonon scattering. The strongest AFM exchange-coupling interaction occurs between Gd atoms via the superexchange path Gd-As-Gd. Our DFT band-structure calculations suggest that GdAsSe is a nodal-line semimetal with an A-type AFM magnetic ground state, compatible with our experimental findings.

ACKNOWLEDGMENTS

R.S. acknowledges the financial support provided by the Ministry of Science and Technology in Taiwan under Projects No. NSTC-111-2124-M-001-007, No. NSTC-110-2112-M-001-065-MY3, and No. NSTC111-2124-M-A49-003 and by Academia Sinica for the budget of AS-iMATE-113-12. The work at SKKU was supported by the National Research Foundation (NRF) of Korea under Grant No. 2020R1A5A1016518. R.S. acknowledges financial support from the Center of Atomic Initiative for New Materials (AI-Mat), National Taiwan University, and from the Featured Areas Research Center Program within the framework of

the Higher Education Sprout Project by the Ministry of Education in Taiwan under Project No. 112L900801. H.-T.J. acknowledges support from the Ministry of Science and Technology, Taiwan, under Grants No. NSTC 112-2112-M-007-034 -MY3 and No. NSTC 112-2124-M-A49-003, from Academia Sinica, Taiwan, under Grant No. AS-iMATE-113-12, and from NCHC, CINC-NTU, and CQTNTHU-MOE, Taiwan. I.P.M. acknowledges the Department of Science and Technology (IN) in India for support from INSPIRE faculty Award No. DST/INSPIRE/04/2016/002275 (IFA16-PH171) and a Banaras Hindu University for Institutes of Eminence (IoE) Seed Grant. I.P.M. also acknowledges the funding by the UGC-DAE Consortium for Scientific Research, Mumbai, India under Project No. CRS/2022-23/03/863 and the Department of Science and Technology, Science and Engineering Research Board (DST-SERB), India through research grants.

The authors declare no competing financial interest.

[1] P. Monçeau, N. P. Ong, A. M. Portis, A. Meerschaut, and J. Rouxel, Electric field breakdown of charge-density-wave-induced anomalies in $NbSe_3$, Phys. Rev. Lett. **37**, 602 (1976).

[2] R. L. Withers and J. A. Wilson, An examination of the formation and characteristics of charge-density waves in inorganic materials with special reference to the two- and one-dimensional transition-metal chalcogenides, J. Phys. C: Solid State Phys. **19**, 4809 (1986).

[3] F. Hulliger, GdPS and related new rare earth compounds, Nature (London). **219**, 373 (1968).

[4] I. P. Muthuselvam, R. Nehru, K. R. Babu, K. Saranya, S. N. Kaul, S. M. Chen, W. T. Chen, Y. Liu, G. Y. Guo, F. Xiu, and R. Sankar, Gd_2Te_3: An antiferromagnetic semimetal, J. Phys.: Condens. Matter **31**, 285802 (2019).

[5] R. Sankar, I. P. Muthuselvam, K. Rajagopal, K. Ramesh Babu, G. S. Murugan, K. S. Bayikadi, K. Moovendaran, C. Ting Wu, and G. Y. Guo, Anisotropic magnetic properties of nonsymmorphic semimetallic single crystal NdSbTe, Cryst. Growth Des. **20**, 6585 (2020).

[6] R. Sankar, I. P. Muthuselvam, K. R. Babu, G. S. Murugan, K. Rajagopal, R. Kumar, T. C. Wu, C. Y. Wen, W. L. Lee, G. Y. Guo, and F. C. Chou, Crystal growth and magnetic properties of topological nodal-line semimetal GdSbTe with antiferromagnetic spin ordering, Inorg. Chem. **58**, 11730 (2019).

[7] M. Hirschberger, S. Kushwaha, Z. Wang, Q. Gibson, S. Liang, C. A. Belvin, B. A. Bernevig, R. J. Cava, and N. P. Ong, The chiral anomaly and thermopower of Weyl fermions in the half-Heusler GdPtBi, Nat. Mater. **15**, 1161 (2016).

[8] S. Borisenko, D. Evtushinsky, Q. Gibson, A. Yaresko, K. Koepernik, T. Kim, M. Ali, J. van den Brink, M. Hoesch, A. Fedorov, E. Haubold, Y. Kushnirenko, I. Soldatov, R. Schäfer, and R. J. Cava, Time-reversal symmetry breaking type-II Weyl state in $YbMnBi_2$, Nat. Commun. **10**, 3424 (2019).

[9] N. Kumar Shekhar, V. Grinenko, S. Singh, R. Sarkar, H. Luetkens, S.-C. Wu, Y. Zhang, A. C. Komarek, E. Kampert, Y. Skourski, J. Wosnitza, W. Schnelle, A. McCollam, U. Zeitler, J. Kübler, B. Yan, H.-H. Klauss, S. S. P. Parkin, and C. Felser, Anomalous Hall effect in Weyl semimetal half-Heusler compounds RPtBi (R = Gd and Nd), Proc. Natl. Acad. Sci. USA **115**, 9140 (2018).

[10] C. K. Barman, P. Singh, D. D. Johnson, and A. Alam, Revealing the nature of antiferroquadrupolar ordering in cerium hexaboride: CeB_6, Phys. Rev. Lett. **122**, 076401 (2019).

[11] P. C. Canfield, New materials physics, Rep. Prog. Phys. **83**, 016501 (2019).

[12] B. Keimer and J. Moore, The physics of quantum materials, Nat. Phys. **13**, 1045 (2017).

[13] G. Xu, B. Lian, and S.-C. Zhang, Intrinsic quantum anomalous Hall effect in the kagome lattice $Cs_2LiMn_3F_{12}$, Phys. Rev. Lett. **115**, 186802 (2015).

[14] X. Duan, F. Wu, J. Chen, P. Zhang, Y. Liu, H. Yuan, and C. Cao, Tunable electronic structure and topological properties of LnPn (Ln = Ce, Pr, Sm, Gd, Yb; Pn = Sb, Bi), Commun. Phys. **1**, 71 (2018).

[15] S. X. M. Riberolles, T. V. Trevisan, B. Kuthanazhi, T. W. Heitmann, F. Ye, D. C. Johnston, S. L. Bud'ko, D. H. Ryan, P. C. Canfield, A. Kreyssig, A. Vishwanath, R. J. McQueeney, L.-L. Wang, P. P. Orth, and B. G. Ueland, Magnetic crystalline-symmetry-protected axion electrodynamics and field-tunable unpinned Dirac cones in $EuIn_2As_2$, Nat. Commun. **12**, 999 (2021).

[16] H. Weng, J. Zhao, Z. Wang, Z. Fang, and X. Dai, Topological crystalline Kondo insulator in mixed valence, ytterbium borides, Phys. Rev. Lett. **112**, 016403 (2014).

[17] N. Wakeham, E. D. Bauer, M. Neupane, and F. Ronning, Large magnetoresistance in the antiferromagnetic semimetal NdSb, Phys. Rev. B **93**, 205152 (2016).

[18] K. Kuroda *et al.*, Devil's staircase transition of the electronic structures in CeSb, Nat. Commun. **11**, 2888 (2020).

[19] P. Li, Z. Wu, F. Wu, C. Cao, C. Guo, Y. Wu, Y. Liu, Z. Sun, C.-M. Cheng, D.-S. Lin, F. Steglich, H. Yuan, T.-C. Chiang, and Y. Liu, Tunable electronic structure and surface states in rare-earth monobismuthides with partially filled f shell, Phys. Rev. B **98**, 085103 (2018).

[20] A. P. Sakhya, B. Wang, F. Kabir, C.-Y. Huang, M. M. Hosen, B. Singh, S. Regmi, G. Dhakal, K. Dimitri, M. Sprague, R. Smith, E. D. Bauer, F. Ronning, A. Bansil, and M. Neupane, Complex electronic structure evolution of NdSb across the magnetic transition, Phys. Rev. B **106**, 235119 (2022).

[21] S. Pakhira, F. Islam, E. O'Leary, M. A. Tanatar, T. Heitmann, L.-L. Wang, R. Prozorov, A. Kaminski, D. Vaknin, and D. C. Johnston, A-type antiferromagnetic order in semiconducting $EuMg_2Sb_2$ single crystals, Phys. Rev. B **106**, 024418 (2022).

[22] J. Ma, H. Wang, S. Nie, C. Yi, Y. Xu, H. Li, J. Jandke, W. Wulfhekel, Y. Huang, D. West, P. Richard, A. Chikina, V. N. Strocov, J. Mesot, H. Weng, S. Zhang, Y. Shi, T. Qian, M. Shi, and H. Ding, Emergence of nontrivial low-energy Dirac fermions in antiferromagnetic $EuCd_2As_2$, Adv. Mater. **32**, 1907565 (2020).

[23] J. Blawat, M. Marshall, J. Singleton, E. Feng, H. Cao, W. Xie, and R. Jin, Unusual electrical and magnetic properties in layered $EuZn_2As_2$, Adv. Quantum Technol. **5**, 2200012 (2022).

[24] Y. Wang *et al.*, Topological semimetal state and field-induced Fermi surface reconstruction in the antiferromagnetic monopnictide NdSb, Phys. Rev. B **97**, 115133 (2018).

[25] B. Schrunk, Y. Kushnirenko, B. Kuthanazhi, J. Ahn, L. L. Wang, E. O'Leary, K. Lee, A. Eaton, A. Fedorov, R. Lou, V. Voroshnin, O. J. Clark, J. Sánchez-Barriga, S. L. Bud'ko, R. J. Slager, P. C. Canfeld, and A. Kaminski, Emergence of Fermi arcs due to magnetic splitting in an antiferromagnet, Nature (London) **603**, 610 (2022).

[26] Y. Kushnirenko, B. Schrunk, B. Kuthanazhi, L.-L. Wang, J. Ahn, E. O'Leary, A. Eaton, S. L. Bud'ko, R.-J. Slager, P. C. Canfeld, and A. Kaminski, Rare-earth monopnictides: Family of antiferromagnets hosting magnetic Fermi arcs, Phys. Rev. B **106**, 115112 (2022).

[27] T. Asaba, S. M. Thomas, M. Curtis, J. D. Thompson, E. D. Bauer, and F. Ronning, Anomalous Hall effect in the kagome ferrimagnet $GdMn_6Sn_6$, Phys. Rev. B **101**, 174415 (2020).

[28] J. X. Yin *et al.*, Quantum-limit Chern topological magnetism in $TbMn_6Sn_6$, Nature (London) **583**, 533 (2020).

[29] P. Schobinger-Papamantellos, J. Rodrłguez-Carvajal, and K. H. J. Buschow, Cycloid spirals and cycloid cone transition in the $HoMn_{6-x}Cr_xGe_6$ (T,x) magnetic phase diagram by neutron diffraction, J. Magn. Magn. Mater. **408**, 233 (2016).

[30] N. J. Ghimire, R. L. Dally, L. Poudel, D. C. Jones, D. Michel, N. T. Magar, M. Bleuel, M. A. Mcguire, J. S. Jiang, J. F. Mitchell, J. W. Lynn, and I. I. Mazin, Competing magnetic phases and fluctuation-driven scalar spin chirality in the kagome metal YMn_6Sn_6, Sci. Adv. **6**, eabe2680 (2020).

[31] M. Li, Q. Wang, G. Wang, Z. Yuan, W. Song, R. Lou, Z. Liu, Y. Huang, Z. Liu, H. Lei, Z. Yin, and S. Wang, Dirac cone, flat band and saddle point in kagome magnet YMn_6Sn_6, Nat. Commun. **12**, 3129 (2021).

[32] B. Wang, E. Yi, L. Li, J. Qin, B.-F. Hu, B. Shen, and M. Wang, Magnetotransport properties of the kagome magnet $TmMn_6Sn_6$, Phys. Rev. B **106**, 125107 (2022).

[33] K. W. Chen, Y. Lai, Y. C. Chiu, S. Steven, T. Besara, D. Graf, T. Siegrist, T. E. Albrecht-Schmitt, L. Balicas, and R. E. Baumbach, Possible devil's staircase in the Kondo lattice CeSbSe, Phys. Rev. B **96**, 014421 (2017).

[34] L. M. Schoop, A. Topp, J. Lippmann, F. Orlandi, L. Müchler, M. G. Vergniory, Y. Sun, A. W. Rost Y, V. Duppel, M. Krivenkov, S. Sheoran, P. Manuel, A. Varykhalov, B. Yan, R. K. Kremer, C. R. Ast, and B. V. Lotsch, Tunable Weyl and Dirac states in the nonsymmorphic compound CeSbTe, Sci. Adv. **4**, eaar2317 (2018).

[35] N. E. Bibler and M. L. Hyder, Radiolysis of chloroform in the intense radiation pulse from a nuclear explosion, Nature (London) **219**, 374 (1968).

[36] R. Schmelczer, D. Schwarzenbach, and F. Z. Hulliger, On the rare-earth pnigochalcogenides LnAsSe, Z. Naturforsch., B: J. Chem. Sci. **36b**, 463 (1981).

[37] F. Q. Huang, P. Brazis, C. R. Kannewurf, and J. A. Ibers, Syntheses, structures, and physical properties of LnAsTe (Ln = La, Pr, Sm, Gd, Dy, Er), Inorg. Chem. **39**, 3176 (2000).

[38] P. Gebauer, H. Poddig, L. T. Corredor-Bohorquez, T. V. Menshchikova, I. P. Rusinov, P. Golub, F. Caglieris, C. Benndorf, T. Lindemann, E. V. Chulkov, A. U. B. Wolter, B. Büchner, T. Doert, and A. Isaeva, Heavy-atom antiferromagnet GdBiTe: An interplay of magnetism and topology in a symmetry-protected topological semimetal, Chem. Mater. **33**, 2420 (2021).

[39] S. Regmi, R. Smith, A. Pradhan Sakhya, M. Sprague, M. I. Mondal, I. B. Elius, N. Valadez, A. Ptok, D. Kaczorowski, and M. Neupane, Observation of gapless nodal-line states in NdSbTe, Phys. Rev. Mater. **7**, 044202 (2023).

[40] G. Kresse and J. Furthmüller, Efficiency of ab-initio total energy calculations for metals and semiconductors using a plane-wave basis set, Comput. Mater. Sci. **6**, 15 (1996).

[41] G. Kresse and J. Furthmüller, Efficient iterative schemes for *ab initio* total-energy calculations using a plane-wave basis set, Phys. Rev. B **54**, 11169 (1996).

[42] J. P. Perdew, J. A. Chevary, S. H. Vosko, K. A. Jackson, M. R. Pederson, D. J. Singh, and C. Fiolhais, Atoms, molecules, solids, and surfaces: Applications of the generalized gradient approximation for exchange and correlation, Phys. Rev. B **46**, 6671 (1992).

[43] J. P. Perdew, K. Burke, and M. Ernzerhof, Generalized gradient approximation made simple, Phys. Rev. Lett. **77**, 3865 (1996).

[44] A. I. Liechtenstein, V. I. Anisimov, and J. Zaanen, Density-functional theory and strong interactions: Orbital ordering in Mott-Hubbard insulators, Phys. Rev. B **52**, R5467(R) (1995).

[45] A. B. Shick, A. I. Liechtenstein, and W. E. Pickett, Implementation of the LDA+U method using the full-potential linearized augmented plane-wave basis, Phys. Rev. B **60**, 10763 (1999); V. I. Anisimov, F. Aryasetiawan, and A. I. Lichtenstein, First-principles calculations of the electronic structure and spectra of strongly correlated systems: the LDA+ U method, J. Phys.: Condens. Matter **9**, 767 (1997); B. T. Thole, G. van der Laan, J. C. Fuggle, G. A. Sawatzky, R. C. Karnatak, and J.-M. Esteva, 3d x-ray-absorption lines and the $3d^94f^{n+1}$ multiplets of the lanthanides, Phys. Rev. B **32**, 5107 (1985).

[46] S. Zhang, R. Xu, N. Luo, and X. Zou, Two-dimensional magnetic materials: Structures, properties and external controls, Nanoscale **13**, 1398 (2021).

[47] P.-F. Chung, V. Balaji, C.-C. Su, J.-T. Chang, H.-K. Cheng, C.-A. Liu, H. Yu, C.-S. Chang, S.-Y. Guan, and T.-M. Chuang, Design and performance of an ultrahigh vacuum spectroscopic-imaging scanning tunneling microscope with a hybrid vibration isolation system, Rev. Sci. Instrum. **95**, 033701 (2024).

[48] C. C. Su, C. S. Li, T. C. Wang, S. Y. Guan, R. Sankar, F. C. Chou, C. S. Chang, W. L. Lee, G. Y. Guo, and T. M. Chuang, Surface termination dependent quasiparticle scattering interference and magneto-transport study on ZrSiS, New J. Phys. **20**, 103025 (2018).

[49] I. P. Muthuselvam, R. Sankar, A. U. Ushakov, G. N. Rao, S. V. Streltsov, and F. C. Chou, Two-step antiferromagnetic transition and moderate triangular frustration in $Li_2Co(WO_4)_2$, Phys. Rev. B **90**, 174430 (2014).

[50] I. P. Muthuselvam, R. Sankar, A. V. Ushakov, W. T. Chen, G. Narsinga Rao, S. V. Streltsov, S. K. Karna, L. Zhao, M. K. Wu, and F. C. Chou, Successive spin orderings of tungstate-bridged $Li_2Ni(WO_4)_2$ of spin 1, J. Phys.: Condens. Matter **27**, 456001 (2015).

[51] D. C. Johnston, Magnetic susceptibility of collinear and noncollinear Heisenberg antiferromagnets, Phys. Rev. Lett. **109**, 077201 (2012).

[52] D. C. Johnston, Unified molecular field theory for collinear and noncollinear Heisenberg antiferromagnets, Phys. Rev. B **91**, 064427 (2015).